On the deposition and polymorphism of CaCO_3 crystals in the presence of the tetrapod-shaped ZnO nanomaterials and polydimethylsiloxane composite

Yamamoto, Natsuki
Cooperative Program for Resources Engineering, Graduate School of Engineering, Kyushu University

Kioka, Arata
Cooperative Program for Resources Engineering, Graduate School of Engineering, Kyushu University

Yamada, Yasuhiro
Cooperative Program for Resources Engineering, Graduate School of Engineering, Kyushu University

出版情報：Results in Surfaces and Interfaces. 12, pp.100138-, 2023-08-01. Elsevier
バージョン：

Results in Surfaces and Interfaces 12 (2023) 100138

Contents lists available at ScienceDirect

Results in Surfaces and Interfaces

journal homepage: www.elsevier.com/locate/rsurfi

On the deposition and polymorphism of $CaCO_3$ crystals in the presence of the tetrapod-shaped ZnO nanomaterials and polydimethylsiloxane composite

Natsuki Yamamoto [a], Arata Kioka [a,b,*], Yasuhiro Yamada [a,b]

[a] Cooperative Program for Resources Engineering, Graduate School of Engineering, Kyushu University, Fukuoka 819-0395, Japan
[b] Department of Earth Resources Engineering, Faculty of Engineering, Kyushu University, Fukuoka 819-0395, Japan

ARTICLE INFO

Keywords:
Calcium carbonate
Hydrophobicity
Polymorphs
Scale inhibition
Zinc oxide nanomaterials

ABSTRACT

The calcium carbonate ($CaCO_3$) scale generated in water pipes and heat exchangers causes serious problems such as pipe blockage and corrosion. This study investigates the effect of the 4-to-10 μm-long and 350-to-700 nm centering-nucleus-wide ZnO tetrapod-like nanomaterials and polydimethylsiloxane composite (t-ZnO/PDMS) on deposition and polymorphism of $CaCO_3$ crystals on the stainless-steel substrate. The results showed that the t-ZnO/PDMS coating inhibited $CaCO_3$ depositions and represented an excellent antifouling coating. The weight-based inhibition efficiencies of $CaCO_3$ deposition were up to 81.3% and 63.2% at 20 °C and 60 °C, respectively. The t-ZnO/PDMS coating also exhibited good inhibition in the presence of liquid flow. The inhibition is primarily because the very fine concave-convex microstructure of the t-ZnO/PDMS coated surface lowered the surface energy of the substrates, making it difficult for $CaCO_3$ crystals to adhere to the surface. Also, metastable vaterite and aragonite precipitations were dominant in the t-ZnO/PDMS coated coupons at 20 °C and 60 °C, respectively, whereas the uncoated coupon exhibited calcite as the predominant polymorph in all the studied conditions. The t-ZnO/PDMS composite subject to the liquid flow made calcites distorted and framboidal vaterite aggregates, likely due to their mechanical effects. The inhibition of $CaCO_3$ depositions is due to achieving hydrophobicity on substrate surfaces, changing preferential polymorph formation, and tailoring the morphology of the given polymorph by the t-ZnO/PDMS composite.

1. Introduction

Calcium carbonate ($CaCO_3$) is among the most abundant minerals on earth, posing important in a broad discipline of studies, including scale formation (MacAdam and Parsons, 2004; Chaussemier et al., 2015), water treatment (Fathi et al., 2006), various interactions with heavy metals (Aziz et al., 2008; Wen et al., 2020), thermal energy storage (Pardo et al., 2014), medicine, drug delivery, orthopedics (Wei et al., 2008; Parakhonskiy et al., 2015; Zhao et al., 2015), durable construction materials (Saulat et al., 2020), biomineralization (Dhami et al., 2013), and global CO_2 cycle (Falkowski et al., 2000). Scale formation or crystallization fouling is an unavoidable problem in water pipes and heat exchangers subjecting to temperature changes (MacAdam and Parsons, 2004; Chaussemier et al., 2015). Scale formation occurs in various locations, from industrial to consumer applications, including industrial water drainage pipes, road and railway tunnels, gas water heaters used in houses, cooling towers and seawater electric field treatment pipes at nuclear power plants, and geothermal power plants (MacAdam and Parsons, 2004; Kioka and Nakagawa, 2021). Given the growing demands of inhibiting $CaCO_3$ scale formations, numerous papers have studied the mechanisms of scale formation and reported effective inhibitors and measures to mitigate $CaCO_3$ depositions at various temperatures and chemical conditions (MacAdam and Parsons, 2004; Chaussemier et al., 2015; Kioka and Nakagawa, 2021; Eichinger et al., 2022). The practical methods of inhibition include (non-)phosphorus chemicals (Tang et al., 2008), polyelectrolyte (Martinod et al., 2008), natural organic molecules, plant extracts (Chaussemier et al., 2015), micro-/nanobubbles (Tagomori et al., 2022; Tegladza et al., 2023; Zhang et al., 2023), and coatings by TiO_2 and SiO_2 nanomaterials (Yan et al., 2007; Ning et al., 2012; Kiaei and Haghtalab, 2014). However, most reported inhibitors and measures were studied in conditions with no flow or very slow liquid flows. This fact implies that seeking effective inhibitors and measures in the presence of liquid flow remains challenging. Advanced nanostructured materials will change the physicochemical properties at the surface and interface of a solid substrate to achieve a high inhibition efficiency even in the presence of liquid flow.

$CaCO_3$ exhibits three crystalline anhydrous polymorphs, including calcite, aragonite, and vaterite, where calcite is the most thermodynamically stable and vaterite is the least stable. $CaCO_3$ also exhibits three hydrous polymorphs; amorphous calcium carbonate (ACC), calcium carbonate monohydrate, and calcium carbonate hexahydrate.

* Corresponding author at: Department of Earth Resources Engineering, Faculty of Engineering, Kyushu University, Fukuoka 819-0395, Japan.
E-mail address: kioka@mine.kyushu-u.ac.jp (A. Kioka).

https://doi.org/10.1016/j.rsurfi.2023.100138
Received 11 June 2023; Received in revised form 15 July 2023; Accepted 21 July 2023

ACC is the least stable non-crystalline polymorph and often acts as the precursor to forming the more stable crystalline polymorphs (Ogino et al., 1987; Gebauer et al., 2008; Rodriguez-Blanco et al., 2011). Controlling precipitation polymorphs should influence the scale system and help mitigate scale formation on the metal surface. For example, metastable vaterite and aragonite polymorphs have a higher specific surface area, solubility, and dispersion than calcite (Naka et al., 2002). However, the polymorph formation and transition, crystal growth, and depositions of $CaCO_3$ depend on chemical and environmental conditions (Oral and Ercan, 2018), hampering a thorough understanding of their mechanisms and providing more universally applicable inhibitors and measures. Among the proposed inhibition methodologies, their effectivities depend primarily on the target materials subject to scale formation (Doyle et al., 2002). Therefore, the advanced nanomaterials applicable to various target materials will be valuable for alternative techniques to mitigate $CaCO_3$ depositions.

Zinc oxide (ZnO) nanomaterials are of great interest due to their widespread utilization in catalysis, dye-sensitized solar cells, sensors, sunscreens, cosmetics, coatings, and optical and electronic materials (Zhang et al., 2008; Ali and Winterer, 2010; Zhou and Keller, 2010). ZnO nanoparticles are one of the most manufactured nanoparticles, and the global production of ZnO nanoparticles is 31,500–34,000 tonnes per year (Keller and Lazareva, 2014). The growing quantities of ZnO nanoparticles are expected to find their way into ecological systems, wastewater treatment, landfill deposition, or other processes. ZnO nanomaterials are generally low-cost, non-toxic, and biocompatible, and their configurations are more copious than any studied nanomaterials, including carbon nanotubes (Wang, 2004). Among various types of ZnO nanomaterials, tetrapod-shaped ZnO (t-ZnO) nanomaterials exhibit a very promising technological potential in broad areas of applications (Wang, 2004). It should also be mentioned that embedding t-ZnO nanomaterials in a polymer, such as the most widely used polymer polydimethylsiloxane (PDMS), improves its wettability features (Zhang et al., 2010; Lee et al., 2011; Mishra and Adelung, 2018; Ghannam et al., 2019), indicating that the t-ZnO-based polymer hydrophobic coatings/paints can be readily developed and mounted on all the industrial equipment that needs to be waterproofed. One of the possible practical measures taken to mitigate scale formation is manipulating the fluid wettability on the substrate surface to prevent scale deposits from adhering to the material surfaces.

However, to our best knowledge, no papers have studied utilizing the hydrophobic features of ZnO to mitigate scale formations. In this work, we investigate the effect of t-ZnO on the precipitation and preferential polymorph formation of $CaCO_3$ crystals by laboratory batch experiments that simulate the conditions, including the presence/absence of liquid flow, temperature, and solution concentration. This paper is the first work revealing that the composite of t-ZnO nanomaterials and polydimethylsiloxane (t-ZnO/PDMS) changes polymorphism and inhibits $CaCO_3$ precipitations. This work sheds new light upon the deposition inhibitions and polymorphism of $CaCO_3$ crystals in the presence of t-ZnO nanomaterials, helping to provide a novel, effective, universally-applicable, and low-cost way to prevent scale formations.

2. Materials and methods

2.1. Experimental setup

The objective of the study is to understand the effect of the t-ZnO/PDMS composite on the deposition and polymorphism of $CaCO_3$ crystals on the stainless-steel substrate using the most simple and generic experiment systems possible. We thus suspended test coupons in surface-contamination-controlled (SCC) pre-cleaned PP bottles (250 mL; AS ONE Corp., Osaka, Japan) using a PTFE string to prevent the coupons from contacting with the bottle walls and bottle bottom. The diameter and height of the bottles were 6.2 cm and 13.0 cm, respectively. We then produced $CaCO_3$ crystal precipitations within the bottles by dissolving sodium hydrogen carbonate $NaHCO_3$ and calcium chloride dihydrate $CaCl_2{\cdot}2H_2O$ (FUJIFILM Wako Pure Chemical Corp., Osaka, Japan) in ultrapure water (PURELAB Flex 3, ELGA, UK). The coupons were immersed in the tested solution with a vertical orientation (Wang et al., 2013). We chose stainless steel as the coupon material because it has corrosion resistance and generates fouling much faster than other candidate materials, such as acrylic and Teflon (Doyle et al., 2002). The coupon was austenitic stainless steel SUS304 ($C \leq 0.08$, $8.0 \leq Ni \leq 10.5$, $18.0 \leq Cr \leq 20.0$, $Si \leq 1.0$, $Mn \leq 2.0$, $P \leq 0.045$, $S \leq 0.030$ wt%, Fe: balance) and its surface area was 11.5 cm^2. The maximum roughness R_z of the tested austenitic stainless-steel coupon was 0.2–0.6 μm by buff polishing with a 400 grit (San-Ai Kagaku Co., Ltd., Nagoya, Japan). We transferred the mixed solution to the bottle and immersed the tested austenitic stainless-steel coupons. We immersed the tested coupons with and without coating the tetrapod-like ZnO single crystals and polydimethylsiloxane (PDMS) composite (t-ZnO/PDMS) for 30, 60, 120, and 180 min under four different experimental conditions. The four experimental conditions were (A) no liquid flow at temperature and concentration of the solution of 20 ± 1.0 °C and 300 mM/L, (B) no liquid flow at 60.0 ± 0.5 °C and 300 mM/L, (C) no liquid flow at 20 ± 1.0 °C and 150 mM/L, and (D) a liquid flow with an equivalent flow velocity at the surface of 39 ± 5 cm/s using a magnetic stirrer at temperature and concentration of the solution of 20.0 ± 1.0 °C and 300 mM/L (Table 1). The pH fell within 5.9 and 6.1 in all the studied conditions.

Table 1
Studied experimental conditions A–D.

Condition	Temperature	Solution concentration	Liquid flow
A	20 ± 1.0 °C	300 mM/L	No (static)
B	60 ± 0.5 °C	300 mM/L	No (static)
C	20 ± 1.0 °C	150 mM/L	No (static)
D	20 ± 1.0 °C	300 mM/L	39 ± 5 cm/s

2.2. Analyses

After immersion of coupons for the respective time of 30, 60, 120, and 180 min, we sampled, washed, and dried the coupons, and calculated the weight changes of coupons in mg/cm^2 (mg of weight change per 1 cm^2 of coupon surface). We confirmed that neither corrosion of the stainless-steel substrate nor abrasion of t-ZnO/PDMS coating was present throughout our experiment. The absolute value of the given weight change was thus identical to the weight of $CaCO_3$ crystals deposited on the coupon surface. The uncertainty in measured weight changes per area arising from reproducibility in our experiment was less than 0.087 mg/cm^2. We also analyzed the $CaCO_3$ crystals precipitated on tested coupons by Scanning Electron Microscope (SEM) using JSM-IT700HR (JEOL, Ltd., Tokyo, Japan) and quantified the fractions of the number and coverage of precipitated crystals and polymorphs of $CaCO_3$. The percentages of the total number and total areal extent of precipitated crystalline anhydrous polymorphs of $CaCO_3$ (calcite, aragonite, and vaterite) were defined by:

$$fN_i = \frac{N_i}{\sum_i N_i} \times 100, \tag{1}$$

$$fA_i = \frac{A_i}{\sum_i A_i} \times 100, \tag{2}$$

where fN_i and fA_i are percentages of the total number and total areal extent of the given polymorph i (i = calcite, aragonite, vaterite), respectively, and N_i and A_i are the total number and total areal extent (μm^2) of the given polymorph i, respectively. The total areal extent A_i was computed using the ImageJ/Fiji software (Schindelin et al., 2012; Schneider et al., 2012).

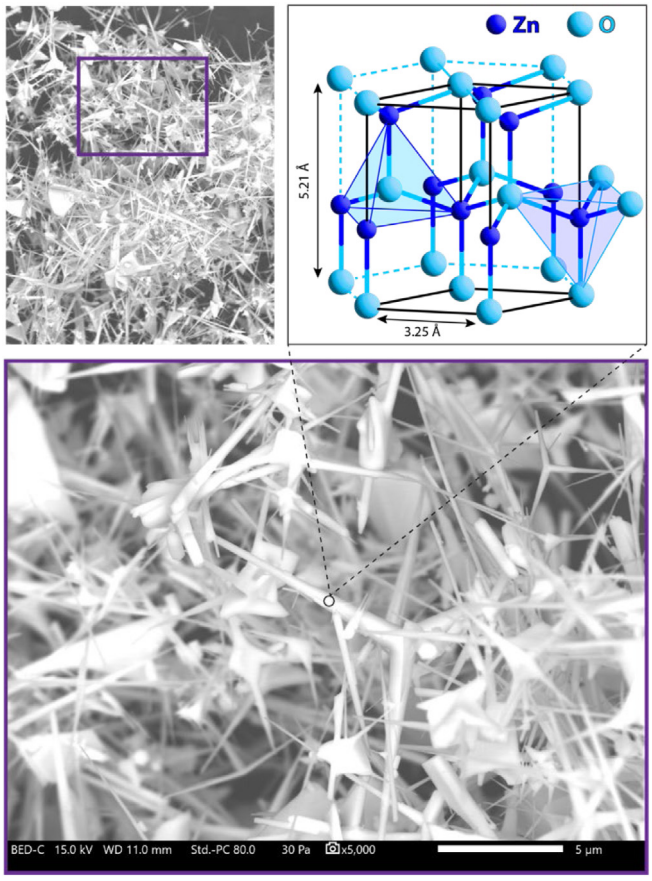

Fig. 1. SEM images of t-ZnO/PDMS composite.

2.3. t-ZnO/PDMS composite coating

We fabricated the t-ZnO/PDMS composite by dissolving tetrapod-shaped ZnO (t-ZnO) nanomaterials (Panatetra-WZ0501; AMSTEC Co., Ltd./Panasonic Industry Co., Ltd., Osaka, Japan) and polydimethylsiloxane (PDMS) room-temperature-vulcanizing silicone (HC2100; Dow Toray Co., Ltd., Tokyo, Japan) to 60 mL of ethyl acetate (FUJIFILM Wako Pure Chemical Corp., Osaka, Japan) and stirring them for 10 min. PDMS is a silicone-based polymer that is transparent, flexible, biocompatible, inexpensive, and easy to use, allowing a wide range of applications. PDMS is also a highly versatile elastomer with outstanding chemical and thermal stability, corrosion resistance, repeatability, chemically inertia, and hyperplastic characteristics (Eduok et al., 2017; Wolf et al., 2018; Ren et al., 2020). The studied t-ZnO nanomaterials are the tetrapod- and needle-shaped crystals grown in the *c*-axis direction of hexagonal ZnO from four alternating faces of each part of the regular octagonal shape (Fig. 1). The length of the legs of t-ZnO single crystals was 4–10 μm, and the typical edge size of the centering nucleus was 350–700 nm, resulting in a slightly acute angle of 5–8°. This tetrapod morphology leads to loose packing with an apparent density of 100 kg/m^3, forming a porous framework with an acicular surface in an elastic PDMS (Fig. 1).

Because ZnO nanomaterials embedded in polymers are known to exhibit hydrophobic behavior (Zhang et al., 2010; Lee et al., 2011; Mishra and Adelung, 2018; Ghannam et al., 2019), selecting an appropriate ratio of t-ZnO and PDMS is essential to achieve hydrophobicity as high as possible. The weight fraction of t-ZnO in the t-ZnO/PDMS composite $f_{t-\mathrm{ZnO}}$ is defined as:

$$f_{\mathrm{t-ZnO}} = \frac{m_{t-\mathrm{ZnO}}}{m_{t-\mathrm{ZnO}} + m_{\mathrm{PDMS}}},$$

where $m_{\mathrm{t-ZnO}}$ and m_{PDMS} are weights of t-ZnO and PDMS in the t-ZnO/PDMS composite. We selected the weight fraction of t-ZnO in the t-ZnO/PDMS composite $f_{t-\mathrm{ZnO}} = 0.5$ (t-ZnO 1.5 g and PDMS 1.5 g) because it presents the best for achieving high water repellence (Yamauchi et al., 2019). We thus performed the coating of the t-ZnO/PDMS composite with $f_{t-\mathrm{ZnO}} = 0.5$ on the stainless-steel coupon and dried it in an oven for 12 h at 40 °C. The coating was evenly spread throughout the coupon surface, and the coating density of t-ZnO/PDMS composite was 55 μL/cm^2 (μL of coating per 1 cm^2 of coupon surface), averaging ~1.4 mg/cm^2 of t-ZnO on the coupon surface. To evaluate the enhanced hydrophobicity due to the t-ZnO/PDMS composite coating, we measured the contact angle of water on the surface by the conventional sessile drop method using 10 μL droplets of ultrapure water. The contact angle on the surface of the austenitic stainless-steel coupon with and without t-ZnO/PDMS coating was 144° and 93° (Fig. 2). Thus, the contact angle increased by approximately 50° due to the t-ZnO/PDMS coating on the stainless-steel substrate, achieving an almost superhydrophobicity (Law, 2014) on the t-ZnO/PDMS coated coupon. The t-ZnO/PDMS composite sustains good hydrophobicity even under the condition subject to unceasing abrasion and bending because of the tetrapod geometry of ZnO and elasticity of PDMS (Yamauchi et al., 2019), promising to maintain the hydrophobic effect for a much longer time than our experiment.

3. Results and discussion

3.1. Weight-based inhibition of $CaCO_3$ depositions

The weight of $CaCO_3$ crystals deposited on the surfaces of uncoated stainless-steel coupons (reference) increased with test time in all the Conditions A – D. The weight per surface area of $CaCO_3$ crystals deposited on the surfaces of uncoated stainless-steel coupons (reference) increased with time, from 0.78 mg/cm^2 (30 min) to 1.92 mg/cm^2 (180 min) and 1.39 mg/cm^2 (30 min) to 1.83 mg/cm^2 (180 min) in Conditions A and B, respectively (Fig. 3a & b). The greater deposition weight in Condition B (60 °C) at 30–120 min is due to the lower dissolubility of $CaCO_3$ with its solution temperature higher than the temperature in Condition A (Plummer and Busenberg, 1982). Also, the weight per surface area of $CaCO_3$ crystals deposited on the uncoated stainless-steel coupons (reference) increased with time, from 0.35 mg/cm^2 (30 min) to 1.39 mg/cm^2 (180 min) and 0.26 mg/cm^2 (30 min) to 0.87 mg/cm^2 (180 min) in Conditions A and B, respectively (Fig. 3c and d). The less deposition weight in Condition D with a lower concentration (150 mM/L) than that in Condition C with a higher concentration (300 mM/L) is because Condition D is subject to liquid flow, encouraging to prevent deposition on the surfaces of stainless steel.

Also, the weight of $CaCO_3$ crystals deposited on the surfaces of the t-ZnO/PDMS coated coupons increased generally with test time in Conditions A – D. However, as compared with the weight of $CaCO_3$ crystals deposited on the uncoated stainless-steel coupons, the t-ZnO/PDMS coated coupons showed less weight of $CaCO_3$ crystals deposited on the coated substrate surface, ranging from 0.35 mg/cm^2 (30 min) to 0.78 mg/cm^2 (180 min) and 0.78 mg/cm^2 (30 min) to 0.87 mg/cm^2 (180 min) in Conditions A and B, respectively (Fig. 3a and b). Likewise, the t-ZnO/PDMS coating also mitigated $CaCO_3$ deposition on the coated substrate surfaces than reference in Conditions C and D (Fig. 3c and d). However, in contrast to the changes observed in the uncoated reference coupons, the t-ZnO/PDMS coated coupons did not necessarily show a monotonical temporal increase in the weight of $CaCO_3$ deposition. For example, the weight per surface area of $CaCO_3$ deposition increased from 30 min to 60 min, reaching 0.96 mg/cm^2, while it dropped to 0.61 mg/cm^2 at 120 min in Condition B (Fig. 3b). These results might indicate that the t-ZnO/PDMS coating restricts the $CaCO_3$ deposition to ~1 mg/cm^2 in all the studied static conditions.

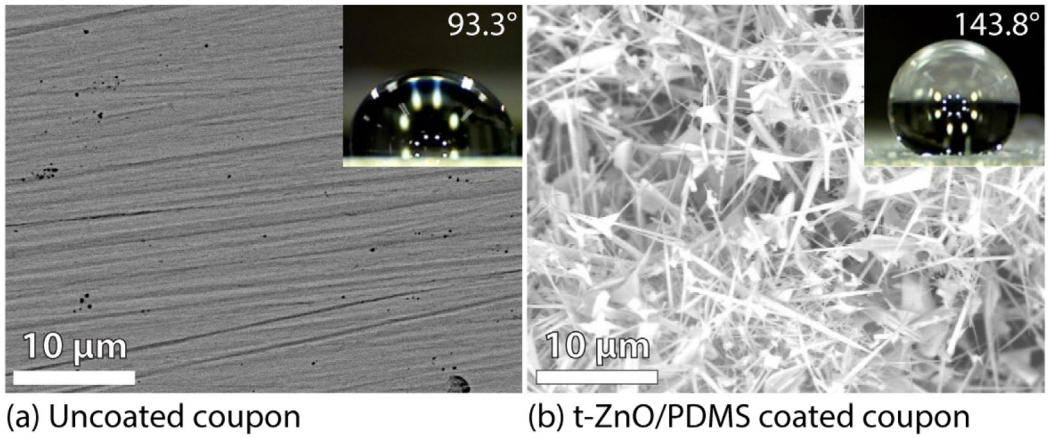

Fig. 2. Increase in contact angle due to t-ZnO/PDMS coating on stainless-steel substrate. The contract angles were measured using 10 µL droplets of ultrapure water at 20 °C.

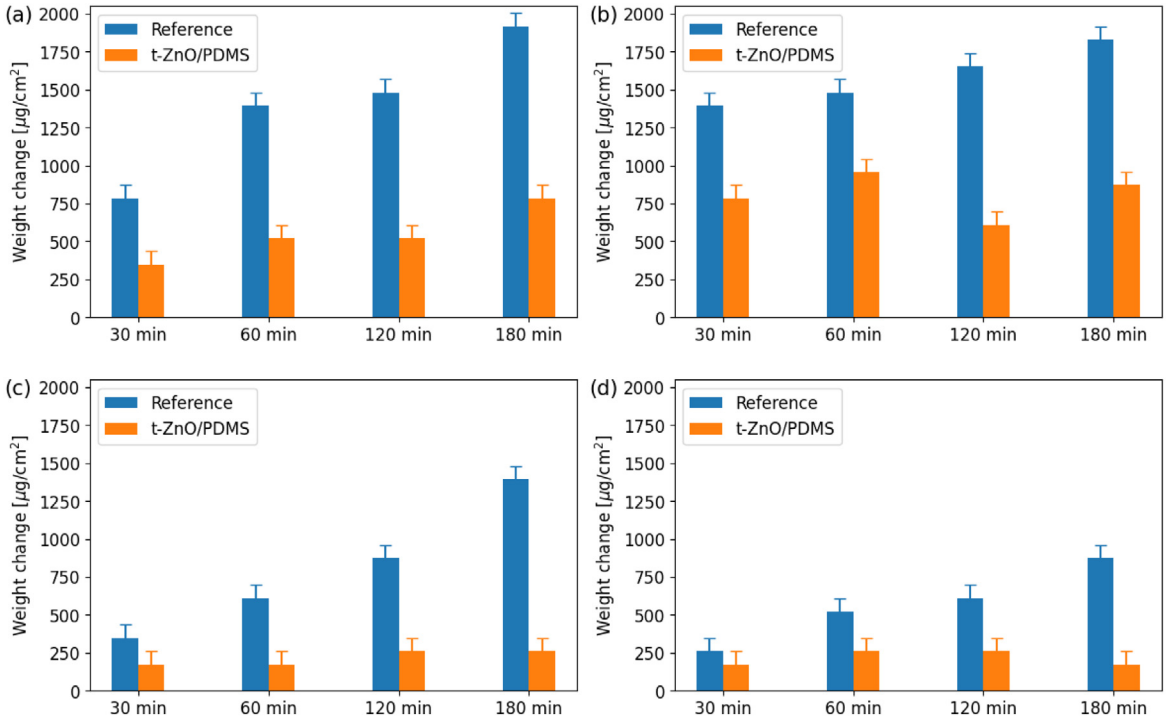

Fig. 3. Weight of $CaCO_3$ crystals (µg/cm^2) deposited on the uncoated stainless-steel coupons ("Reference") and t-ZnO/PDMS coated coupons. (a) Condition A, (b) Condition B, (c) Condition C, (d) Condition D.

These results revealed that the t-ZnO/PDMS coating shows good weight-based inhibition of $CaCO_3$ deposition. The averaged inhibition efficiencies throughout the tested time of 180 min due to the t-ZnO/PDMS coating in Conditions A – D were 60.5%, 48.6%, 68.2%, and 55.1%, respectively (Fig. 4). The inhibition efficiency in Condition B was most inferior, ranging from 35.3(–10.3/+9.2)% to 63.2(–7.6/+6.8)% at the respective time, suggesting that the weight-based inhibition performance by t-ZnO/PDMS composite is less significant with higher temperatures. However, the inhibition efficiency was generally better with time in all the studied conditions, perhaps indicative of better inhibition performance with larger sizes of deposited crystals. Notably, the inhibition efficiency was considerably enhanced with time in Condition D, achieving up to 80.1(–13.3/+10.9)% at 180 min (Fig. 4). This result should highlight that the t-ZnO/PDMS coating is well durable against liquid flows, allowing to have the advantage of being able to mitigate the $CaCO_3$ deposition even in the presence of liquid flows.

The divalent zinc cation Zn^{2+} has inhibition effects on $CaCO_3$ precipitation by reducing the nuclei sites and interfering in the growth stages of $CaCO_3$ crystallization (Sabzi and Arefinia, 2019) and/or delaying the precipitations due to the cation interaction with hydroxide anions OH^- (Benslimane et al., 2020). Previous studies showed that ZnO nano- and microparticles dissolve readily under acidic and alkaline conditions; however, their dissolution is limited under the neutral conditions we studied (Bian et al., 2011; Wu et al., 2019). We thus examined inhibitory effects on the $CaCO_3$ precipitations by t-ZnO alone if its dissolution to a solution is sufficient to have the inhibition effects. Below, we investigated the effect of possible Zn^{2+} ions leached from t-ZnO/PDMS coatings on the $CaCO_3$ deposition. We added 100 mg of t-ZnO powders (approximately 10 times more than the weight of t-ZnO in the given t-ZnO/PDMS coated coupon) to the 300 mM/L $NaHCO_3$+$CaCl_2{\cdot}2H_2O$ solution at 20 °C (identical to Condition A), and then immersed the uncoated stainless-steel coupons in the resulting solution. The results showed that the weight of $CaCO_3$ crystals deposited on coupons was rather 1.05–1.14 times higher than those in Condition

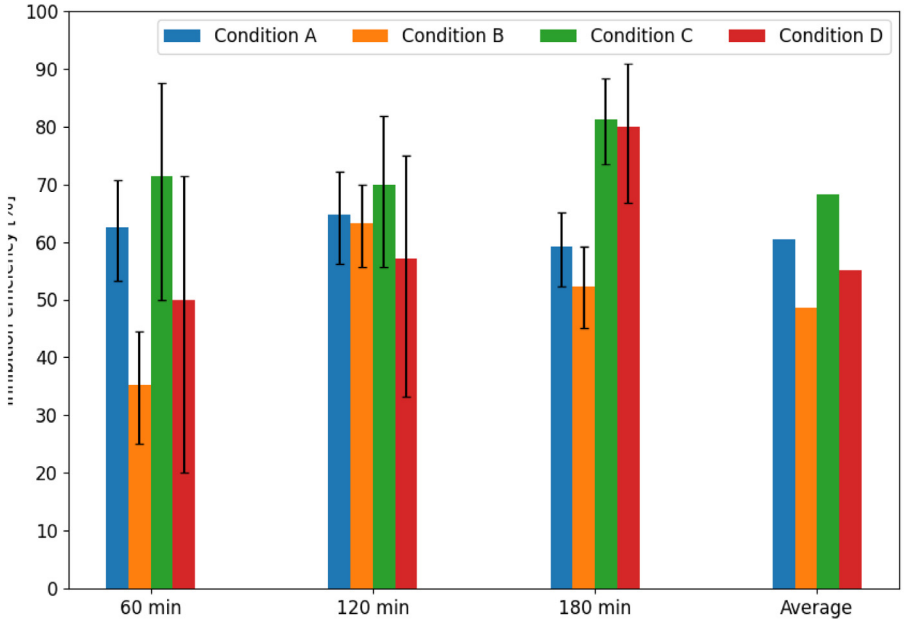

Fig. 4. Inhibition efficiency due to t-ZnO/PDMS coating.

A shown earlier. Therefore, we concluded that the effect of possible Zn^{2+} ions leached from t-ZnO/PDMS composite is either negligible on the tested $CaCO_3$ inhibition, likely with very limited Zn dissolution in the solution at studied pH of ~6, or instead promoting the $CaCO_3$ precipitations.

Having ruled out the possible effect of Zn^{2+} from t-ZnO/PDMS composite on the $CaCO_3$ depositions in our experiment, we discuss the water repellency due to the t-ZnO/PDMS coating that allowed inhibiting the depositions. The nearly superhydrophobicity is achieved due to the t-ZnO/PDMS coating, as found in the contact angle measurement (Fig. 2). When a solid surface is rough, a hydrophobic solid becomes more hydrophobic, and a hydrophilic solid enhances hydrophilicity (Quéré, 2008). The t-ZnO, a tetrapod-shaped needle single crystal, makes the surface roughness of the coated surface very large due to the numerous needles protruding from its surface. Thus, the increase in surface roughness reduces the surface energy of the solid surface, making it difficult for $CaCO_3$ crystal nuclei and tiny crystals to adhere to the substrate surface, resulting in the inhibition effect. This effect is also identified from the results in Condition D, which showed better inhibition efficiency with time in the presence of liquid flow (Fig. 4). The results indicate that the water repellency due to t-ZnO/PDMS coating functions well and leads to mitigating $CaCO_3$ depositions in the presence of liquid flow. This inhibition effectiveness in the presence of liquid flow should be one of the most significant advantages of using t-ZnO/PDMS coating among the reported inhibition techniques that most have difficulties in the presence of liquid flow due to their abrasion and adhesion. The formation of (nearly-)superhydrophobic surface is shown in any substrates (Yamauchi et al., 2019) such as aluminium, glass, rubber, carbon steel, and stainless steel we studied. Stainless steel generally exhibits among the most inferior adhesion of the coating to the material surfaces (Yamauchi et al., 2019), partly due to relatively smooth surface and low interaction with the native oxide layers such as the CrO_2 passive layer (Miyauchi et al., 2016). Nevertheless, our results showed good inhibition even in the stainless steel due to the durability of t-ZnO/PDMS composite, as evidenced by its outstanding abrasion resistance (Yamauchi et al., 2019). We now expect that the metal materials yielding excellent coating adhesion, such as low-carbon steels commonly used for pipes, better withstand abrasion due to liquid flow and show comparable or higher inhibition efficiencies. We thus suggest that t-ZnO/PDMS composite has the advantages of wear resistance and low cost, promising that its practical application can be an effective means of helping to solve $CaCO_3$ scale problems in the broad industrial fields.

Surface roughness of the substrate exerts a significant effect on the deposition, detachment, and growth of $CaCO_3$ crystal (Keysar et al., 1994; Løge et al., 2022). Thus, the weight-based inhibition of $CaCO_3$ deposition due to the t-ZnO/PDMS composite (Figs. 3 and 4) may intuitively be attributed to the reduction in the number and size of $CaCO_3$ crystals deposited on the surfaces of t-ZnO/PDMS coated coupons. SEM images allowed us to quantify the sizes of $CaCO_3$ crystals deposited on the reference and t-ZnO/PDMS coated substrates (Fig. 5). For example, the crystal sizes of calcite (reference coupon, t-ZnO/PDMS-coated coupon) at 120 min were (15–20, 20–25) μm, (15–20, 15–20) μm, (10–15, 10–15) μm, and (5–10, 5–10) μm in Conditions A, B, C, and D, respectively. We thus identified no significant differences in crystal sizes between reference and t-ZnO/PDMS coated coupons. In contrast, SEM images revealed the difference in the number of $CaCO_3$ crystal precipitations on the reference and t-ZnO/PDMS coated coupons (Fig. 5). The t-ZnO/PDMS composite reduced the number of $CaCO_3$ crystals deposited on the coupons throughout the test time, accounting for the high efficiency in the weight-based inhibition by the t-ZnO/PDMS coatings. The air "pocket" facilitated within the submerged microstructure of t-ZnO/PDMS coating might prevent crystals from coming into contact with the liquid phase in the early stages of crystal formation. Although this paper studied the most common scale composition $CaCO_3$, we expect that the t-ZnO/PDMS coating could also help to mitigate other scale depositions (e.g., $MgCO_3$, $BaSO_4$, $CaSO_4$, $MgSO_4$) due to its hydrophobicity.

3.2. Preferential formation of crystalline polymorphs

$CaCO_3$ nucleation is induced when a solution of Ca^{2+} and CO_3^{2-} ions have become supersaturated, and the most soluble ACC ($-\log K_{sp} = 6.4$) is rapidly formed and transformed into the least stable vaterite crystals ($-\log K_{sp} = 7.91$), followed by aragonite ($-\log K_{sp} = 8.34$) or the most stable calcite ($-\log K_{sp} = 8.48$) (Plummer and Busenberg, 1982). The lower solubility product constant K_{sp} values of vaterite and aragonite indicate that obtaining these polymorphs is challenging due to their thermodynamic instability. However, the preferential formation of different crystalline anhydrous polymorphs and the transformation of ACC into crystalline polymorphs depend strongly on the temperature, pH, and saturation level of the solution. For

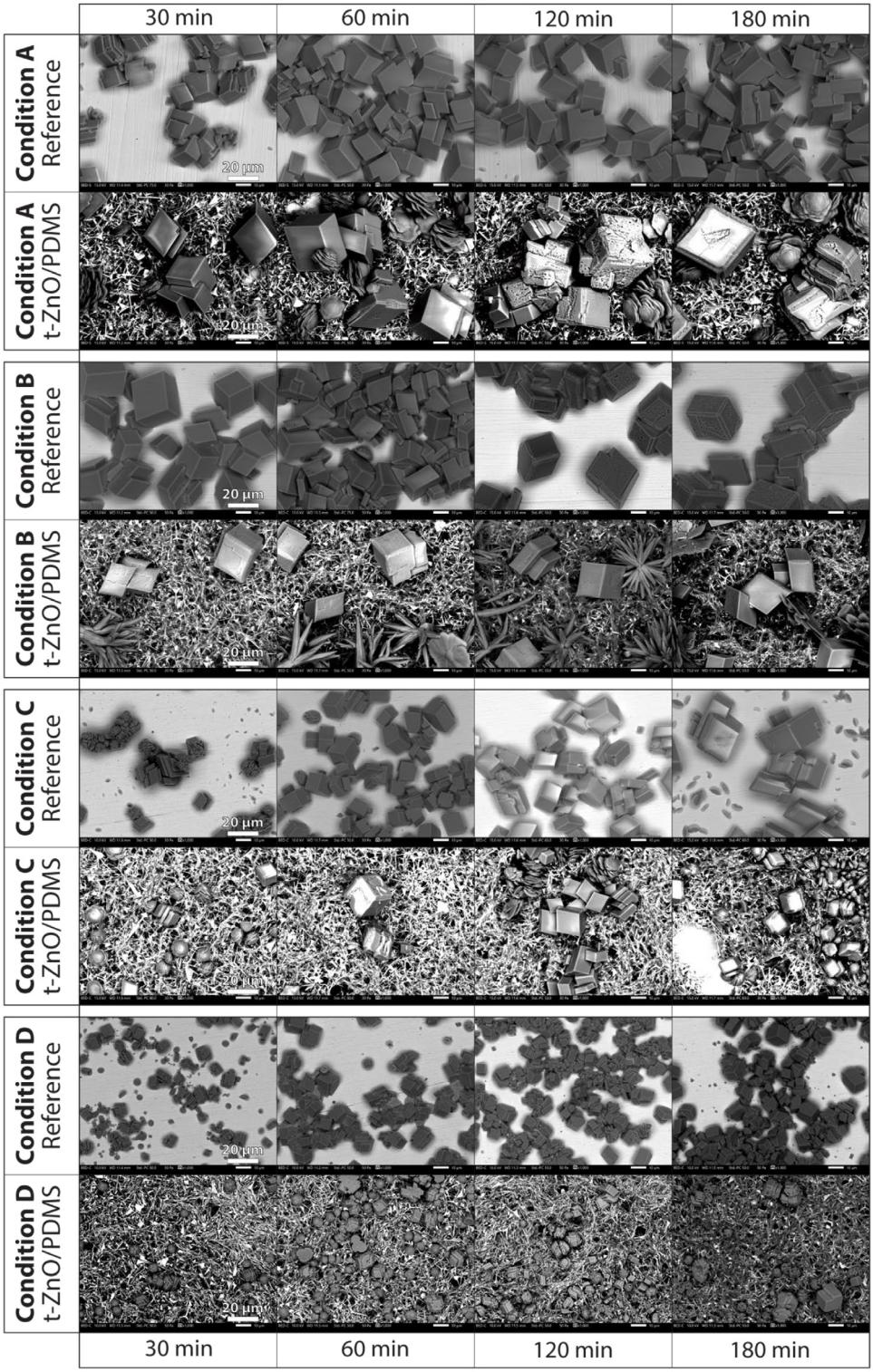

Fig. 5. SEM images of $CaCO_3$ precipitations at Conditions A–D. Whitish needle-like materials on the t-ZnO/PDMS coated coupons are t-ZnO nanomaterials.

example, higher temperature increases the energy of the reactive environment, which favors the formation of high surface energy aragonite crystals from the phase transformation of calcite and vaterite (Boyjoo et al., 2014). Other than temperature, pH, and saturation level of the solution, the material and surface roughness of substrates are the essential factors determining the preferential formation of crystalline anhydrous $CaCO_3$ polymorphs on the substrate surfaces (Wang et al., 2013; Cheong et al., 2013; Karoui et al., 2013). In our experiment, the solution temperature and the substrate surface condition are among the most significant factors determining the preferential polymorph formations. For example, only calcites were deposited on the reference coupons at 20 °C (Conditions A, C, and D), while a few aragonites were deposited at a higher temperature of 60 °C (Condition B) on the reference coupons (Fig. 5). These results agree with earlier studies on the stainless-steel substrates we studied (Wang et al., 2013). The high proportion of calcite crystals on the surface of the stainless steel is due to the stability of calcite crystals at conditions of low temperature and high supersaturation. The calcites deposited on the reference coupons

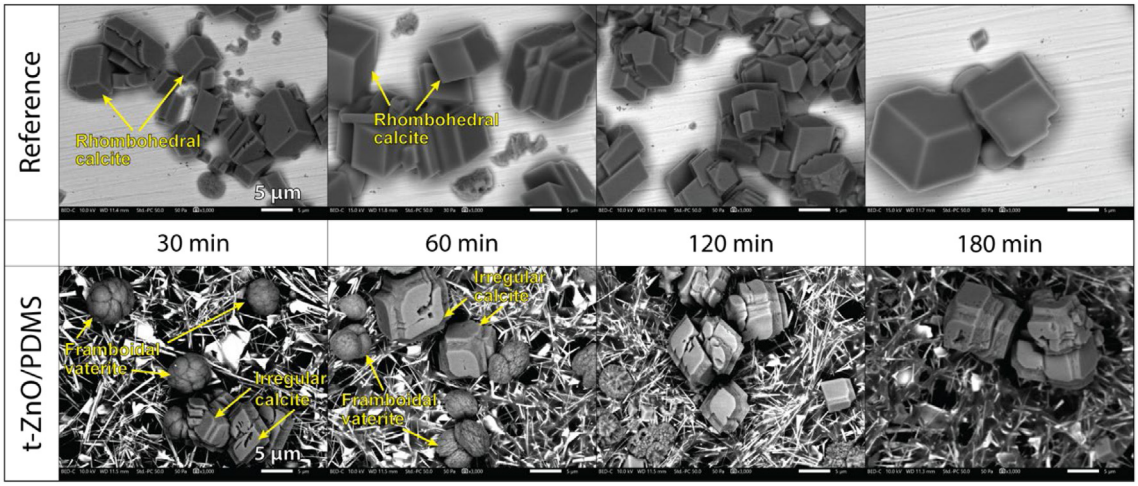

Fig. 6. SEM images of $CaCO_3$ polymorphs precipitated on the uncoated stainless-steel coupons ("Reference") and t-ZnO/PDMS coated coupons at Condition D. Whitish needle-like materials on the t-ZnO/PDMS coated coupons are t-ZnO nanomaterials.

were typical rhombohedral crystals in all the studied conditions (Figs. 5 and 6).

In contrast, the $CaCO_3$ deposition on the t-ZnO/PDMS coated coupons differed significantly from those on the reference coupons. At 20 °C with Conditions A and C, flowerlike vaterites were present more than calcites (Fig. 5), accounting for $\left(fN_{vaterite}, fA_{vaterite}\right) = (65.9, 75.0)\%$ and $\left(fN_{vaterite}, fA_{vaterite}\right) = (79.8, 79.2)\%$ in Conditions A and C, respectively (Fig. 7). This indicates that the thermodynamically less stable vaterite is stabilized on the t-ZnO/PDMS coating, although calcite is thermodynamically most stable under the studied ambient condition. As suggested by the earlier studies of scale inhibitors (Gopi et al., 2013), more vaterite can be present in the scale deposits when the scale inhibition is more efficient. This is likely because the t-ZnO/PDMS coating interferes with the growing sites of the given crystal, preventing the growth of vaterite, while blocking the sites inhibits the dissolution of vaterite as they also serve as active dissolution sites. These mechanisms could impede the transformation from metastable vaterite to stable calcite. Thus, the predominance of metastable vaterite rather than calcite agreed with achieving the greatest inhibition effectiveness in Conditions A and C (Fig. 4). On the other hand, vaterites were less present than calcites in the presence of liquid flow at the same temperature of 20 °C (Condition D), yielding the percentages of $\left(fN_{vaterite}, fA_{vaterite}\right) = (47.9, 33.0)\%$. The lower percentage of vaterite in coverage fraction ($fA_{vaterite}$) than that in number fraction ($fN_{vaterite}$) in Condition D is due to more spheroid-like shapes minimizing the 2D coverage area in SEM images (see Section 3.2). At 60 °C (Condition B), the depositions of aragonites in the form of flowerlike radiating aggregates were predominant on the t-ZnO/PDMS coated coupons (Fig. 5), which were 7.3–8.8 times more total number and areal extent than the reference coupons (Fig. 7). These polymorph compositions of $CaCO_3$ crystals precipitated on the t-ZnO/PDMS coated coupons followed as a well-known function of temperature (Ogino et al., 1987; Trushina et al., 2014); i.e., initial ACC transform to the combination of vaterite and calcite at low temperatures and vaterite can occur predominantly at around 20 °C, whereas elevated temperatures perhaps above 50–60 °C stabilize aragonite polymorph. Therefore, the t-ZnO/PDMS composite significantly counteracted the effect of leached ions in the stainless-steel substrate. The possible presence of cation impurity Zn^{2+} leached from the t-ZnO/PDMS composite might help favor the formation of aragonite (Meyer, 1984; Wada et al., 1995; Coetzee et al., 1998). The lowest weight-based inhibition efficiency in Condition B among the four studied conditions (Fig. 4) can attribute partly to the predominance of aragonite, which has a higher specific gravity than calcite ($\rho_{\text{aragonite}} = 2.94$ g/cm^3, $\rho_{\text{calcite}} = 2.71$ g/cm^3) (Christy, 2017). The predominance of aragonite might also result in hampering the $CaCO_3$ deposition on the t-ZnO/PDMS coating with no greater than ~1 mg/cm^2 in Condition B (Fig. 3) due to a large surface area of aragonite per coating area.

It is also noteworthy to report our interesting findings of calcite and vaterite crystals in the presence of the t-ZnO/PDMS composite with the liquid flow (Condition D). In Condition D, the t-ZnO/PDMS composite exhibited the formation of heterogeneous and distorted calcites rather than homogeneous rhombohedral calcites (Fig. 6). The presence of heterogeneous and distorted calcites should be attributed to the presence of liquid flow because they were not identified in Conditions A–C. Some distorted calcites might demonstrate the repair/re-expression of rhombohedral surfaces when crystals were allowed to grow after any growth interference in their earlier stage (DeOliveira and Laursen, 1997). The distortion in calcite crystals was studied by the adsorption of inhibitory substances to the active faces of growing nuclei (Al-Hamzah et al., 2014). However, many distorted calcites identified on the t-ZnO/PDMS coated coupons in Condition D had crack-like structures, 10's nm-to-1 μm width holes on the growth face (1 0 4), and vague corners and edges of crystals (Fig. 6). Thus, we suggest that liquid flow encouraged calcite crystals to continuously contact sharp edges and rods of needle-like t-ZnO nanomaterials allowing calcite crystals to be more distorted mechanically. Moreover, the t-ZnO/PDMS composite in Condition D formed framboidal or cauliflower-like vaterite aggregates (Nehrke and Van Cappellen, 2006; Zhou et al., 2010) rather than flowerlike vaterites identified in the absence of liquid flow (Conditions A – C). At 20 °C the presence of t-ZnO/PDMS composite favors the formation of vaterite over calcite and aragonite. The lower percentage of vaterite in coverage fraction ($fA_{vaterite}$) and number fraction ($fN_{vaterite}$) in Condition D than the percentages in Conditions A and B at the same temperature (Fig. 7) can be due to the vaterite aggregates with spherical/framboidal structure subjecting to detach more readily than calcite. The framboidal or cauliflower-like vaterite aggregates were identified in earlier studies that obtained the vaterite aggregates at similar pH and temperatures (Wei et al., 2008; Zhou and Keller, 2010; Nehrke and Van Cappellen, 2006; Andreassen and Hounslow, 2004), whereas the vaterite aggregates were not identified in Conditions A – C. We thus suggest that the deposited vaterites were subject to rolling over the needle-like uneven microstructure of t-ZnO/PDMS composite, tailoring the morphology of the vaterite aggregates more rounded, although more definitive studies are necessary to investigate the morphological controls due to t-ZnO/PDMS composite.

4. Conclusions

This paper studied the influence of the 4–10 μm-long and 350–700 nm centering-nucleus-wide ZnO tetrapod-shaped nanomaterials

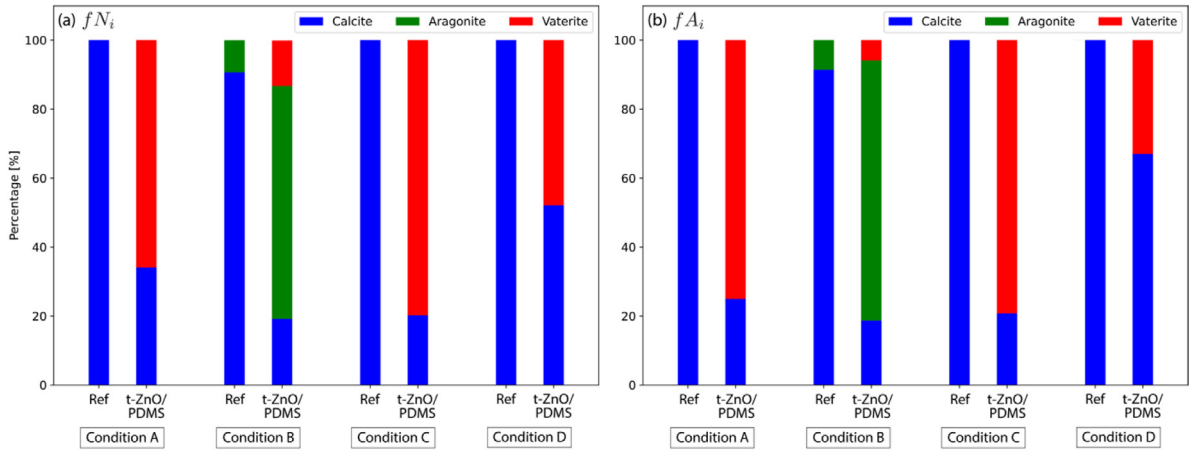

Fig. 7. (a) Percentages of total number fN_i of the given polymorph i (i = calcite, aragonite, vaterite) at 180 min in Conditions A – D. (b) Percentages of total areal extent fA_i of the given polymorph i (i = calcite, aragonite, vaterite) at 180 min in Conditions A – D.

and polydimethylsiloxane composite (t-ZnO/PDMS) on the deposition of 5–25 μm sized $CaCO_3$ polymorphs (calcite, aragonite, and vaterite) on the stainless-steel substrate. The stainless-steel coupons were coated with t-ZnO/PDMS composite and were immersed for 30, 60, 120, and 180 min. We evaluated the weight of $CaCO_3$ precipitations and fractions of the $CaCO_3$ polymorphs deposited on the coupon surfaces under different immersion conditions, including the presence and absence of liquid flow, temperature, and $CaCO_3$ concentration. Our results showed that the t-ZnO/PDMS coating inhibited the $CaCO_3$ depositions under all studied conditions, representing an excellent abrasion-resistant antifouling coating. The average weight-based inhibition effectiveness was 60.5% at 20 °C, 48.7% at 60 °C, 55.1% at 20 °C with a liquid flow, and 68.2% in a 50% concentration of the other tested solutions. The inhibition effectiveness was generally more significant with a longer immersion time, with up to 80.1(–13.3/+10.9)% at 180 min in the presence of liquid flow. We suggest that the very fine concave-convex microstructure of the t-ZnO/PDMS coating surface lowered the surface energy of the coupons, making it difficult for crystals to adhere to the surface and resulting in the inhibition effect. Also, calcite was predominant on the uncoated stainless-steel coupons; however, metastable vaterite and aragonite were dominant polymorphs on the t-ZnO/PDMS coated coupons at 20 °C and 60 °C, respectively, suggesting that the t-ZnO/PDMS composite counteracted the effect of leached ions from the substrate material. The t-ZnO/PDMS composite in the presence of liquid flow made calcites distorted and precipitated framboidal vaterite aggregates, likely due to the mechanical effects benefiting from the very-fine concavity-and-convexity microstructure of t-ZnO/PDMS composite. We conclude that the inhibition of $CaCO_3$ depositions is due to achieving hydrophobicity on substrate surfaces, changing preferential polymorph formation, and tailoring the morphology of the given polymorph by the t-ZnO/PDMS composite. This work sheds new light on the deposition inhibitions and polymorphism of $CaCO_3$ crystals in the presence of t-ZnO/PDMS composite, providing a novel, effective, universally-applicable, and low-cost coating to prevent $CaCO_3$ scale formations.

CRediT authorship contribution statement

Natsuki Yamamoto: Conceptualization, Data curation, Formal analysis, Investigation, Validation, Visualization, Writing – review & editing. **Arata Kioka:** Conceptualization, Data curation, Formal analysis, Funding acquisition, Methodology, Resources, Supervision, Visualization, Writing – original draft. **Yasuhiro Yamada:** Supervision.

Declaration of competing interest

The authors declare that they have no known competing financial interests or personal relationships that could have appeared to influence the work reported in this paper.

Data availability

Data will be made available on request.

Acknowledgments

The authors thank M. Watanabe and R. Yamashiro for assisting the SEM measurement and experiment preparation. This work was supported by JSPS KAKENHI Grant-in-Aid for Early-Career Scientists, Japan (JP21K14576).

Funding

JSPS KAKENHI Grant-in-Aid for Early-Career Scientists, Japan (JP21K14576).

References

Al-Hamzah, A.A., East, C.P., Doherty, W.O.S., Fellows, C.M., 2014. Inhibition of homogenous formation of calcium carbonate by poly (acrylic acid). The effect of molar mass and end-group functionality. Desalination 338, 93–105. http://dx.doi.org/10.1016/j.desal.2014.01.020.

Ali, M., Winterer, M., 2010. ZnO nanocrystals: Surprisingly 'alive'. Chem. Mater. 22, 85–91. http://dx.doi.org/10.1021/cm902240c.

Andreassen, J.-P., Hounslow, M.J., 2004. Growth and aggregation of vaterite in seeded-batch experiments. AIChE J. 50, 2772–2782. http://dx.doi.org/10.1002/aic.10205.

Aziz, H.A., Adlan, M.N., Ariffin, K.S., 2008. Heavy metals (Cd, Pb, Zn, Ni, Cu and Cr(III))removal from water in Malaysia: Post treatment by high quality limestone. Bioresour. Technol. 99, 1578–1583. http://dx.doi.org/10.1016/j.biortech.2007.04.007.

Benslimane, S., Bouhidel, K.-E., Ferfache, A., Farhi, S., 2020. Mechanistic study of the synergetic inhibiting effects of Zn^{2+}, Cu^{2+} and Mg^{2+} ions on calcium carbonate precipitation. Water Res. 186, 116323. http://dx.doi.org/10.1016/j.watres.2020.116323.

Bian, S.-W., Mudunkotuwa, I.A., Rupasinghe, T., Grassian, V.H., 2011. Aggregation and dissolution of 4 nm ZnO nanoparticles in aqueous environments: Influence of pH, ionic strength, size, and adsorption of humic acid. Langmuir 27, 6059–6068. http://dx.doi.org/10.1021/la200570n.

Boyjoo, Y., Pareek, V.K., Liu, J., 2014. Synthesis of micro and nano-sized calcium carbonate particles and their applications. J. Mater. Chem. A 2, 14270–14288. http://dx.doi.org/10.1039/C4TA02070G.

Chaussemier, M., Pourmohtasham, E., Gelus, D., Pécoul, N., Perrot, H., Lédion, J., Cheap-Charpentier, H., Horner, O., 2015. State of art of natural inhibitors of calcium carbonate scaling, A review article. Desalination 356, 47–55. http://dx.doi.org/10.1016/j.desal.2014.10.014.

Cheong, W.C., Gaskell, P.H., Neville, A., 2013. Substrate effect on surface adhesion/crystallisation of calcium carbonate. J. Cryst. Growth 363, 7–21. http://dx.doi.org/10.1016/j.jcrysgro.2012.09.025.

Christy, A.G., 2017. A review of the structures of vaterite: The impossible, the possible, and the likely. Cryst. Growth Des. 17, 3567–3578. http://dx.doi.org/10.1021/acs.cgd.7b00481.

Coetzee, P., Yacoby, M., Howell, S., Mubenga, S., 1998. Scale reduction and scale modification effects induced by Zn and other metal species in physical water treatment. Water SA 24, 77–84.

DeOliveira, D.B., Laursen, R.A., 1997. Control of calcite crystal morphology by a peptide designed to bind to a specific surface. J. Am. Chem. Soc. 119, 10627–10631. http://dx.doi.org/10.1021/ja972270w.

Dhami, N.K., Reddy, M.S., Mukherjee, A., 2013. Biomineralization of calcium carbonates and their engineered applications: a review. Front. Microbiol. 4, http://dx.doi.org/10.3389/fmicb.2013.00314.

Doyle, J.D., Oldring, K., Churchley, J., Parsons, S.A., 2002. Struvite formation and the fouling propensity of different materials. Water Res. 36, 3971–3978. http://dx.doi.org/10.1016/S0043-1354(02)00127-6.

Eduok, U., Faye, O., Szpunar, J., 2017. Recent developments and applications of protective silicone coatings: A review of PDMS functional materials. Prog. Org. Coat. 111, 124–163. http://dx.doi.org/10.1016/j.porgcoat.2017.05.012.

Eichinger, S., Boch, R., Leis, A., Baldermann, A., Domberger, G., Schwab, C., Dietzel, M., 2022. Green inhibitors reduce unwanted calcium carbonate precipitation: Implications for technical settings. Water Res. 208, 117850. http://dx.doi.org/10.1016/j.watres.2021.117850.

Falkowski, P., Scholes, R.J., Boyle, E., Canadell, J., Canfield, D., Elser, J., Gruber, N., Hibbard, K., Högberg, P., Linder, S., Mackenzie, F.T., Moore, B., Pedersen, T., Rosenthal, Y., Seitzinger, S., Smetacek, V., Steffen, W., 2000. The global carbon cycle: A test of our knowledge of earth as a system. Science 290, 291–296. http://dx.doi.org/10.1126/science.290.5490.291.

Fathi, A., Mohamed, T., Claude, G., Maurin, G., Mohamed, B.A., 2006. Effect of a magnetic water treatment on homogeneous and heterogeneous precipitation of calcium carbonate. Water Res. 40, 1941–1950. http://dx.doi.org/10.1016/j.watres.2006.03.013.

Gebauer, D., Völkel, A., Cölfen, H., 2008. Stable prenucleation calcium carbonate clusters. Science 322, 1819–1822. http://dx.doi.org/10.1126/science.1164271.

Ghannam, H., Chahboun, A., Turmine, M., 2019. Wettability of zinc oxide nanorod surfaces. RSC Adv. 9, 38289–38297. http://dx.doi.org/10.1039/C9RA05378F.

Gopi, S., Subramanian, V.K., Palanisamy, K., 2013. Aragonite–calcite–vaterite: A temperature influenced sequential polymorphic transformation of CaCO3 in the presence of DTPA. Mater. Res. Bull. 48, 1906–1912. http://dx.doi.org/10.1016/j.materresbull.2013.01.048.

Karoui, H., Riffault, B., Jeannin, M., Kahoul, A., Gil, O., Ben Amor, M., Tlili, M.M., 2013. Electrochemical scaling of stainless steel in artificial seawater: Role of experimental conditions on CaCO3 and Mg(OH)2 formation. Desalination 311, 234–240. http://dx.doi.org/10.1016/j.desal.2012.07.011.

Keller, A.A., Lazareva, A., 2014. Predicted releases of engineered nanomaterials: From global to regional to local. Environ. Sci. Technol. Lett. 1, 65–70. http://dx.doi.org/10.1021/ez400106t.

Keysar, S., Semiat, R., Hasson, D., Yahalom, J., 1994. Effect of surface roughness on the morphology of calcite crystallizing on mild steel. J. Colloid Interface Sci. 162, 311–319. http://dx.doi.org/10.1006/jcis.1994.1044.

Kiaei, Z., Haghtalab, A., 2014. Experimental study of using Ca-DTPMP nanoparticles in inhibition of CaCO3 scaling in a bulk water process. Desalination 338, 84–92. http://dx.doi.org/10.1016/j.desal.2014.01.027.

Kioka, A., Nakagawa, M., 2021. Theoretical and experimental perspectives in utilizing nanobubbles as inhibitors of corrosion and scale in geothermal power plant. Renew. Sustain. Energy Rev. 149, 111373. http://dx.doi.org/10.1016/j.rser.2021.111373.

Law, K.-Y., 2014. Definitions for hydrophilicity, hydrophobicity, and superhydrophobicity: Getting the basics right. J. Phys. Chem. Lett. 5, 686–688. http://dx.doi.org/10.1021/jz402762h.

Lee, M., Kwak, G., Yong, K., 2011. Wettability control of ZnO nanoparticles for universal applications. ACS Appl. Mater. Interfaces 3, 3350–3356. http://dx.doi.org/10.1021/am2004762.

Løge, I.A., Bentzon, J.R., Klingaa, C.G., Walther, J.H., Anabaraonye, B.U., Fosbøl, P.L., 2022. Scale attachment and detachment: The role of hydrodynamics and surface morphology. Chem. Eng. J. 430, 132583. http://dx.doi.org/10.1016/j.cej.2021.132583.

MacAdam, J., Parsons, S.A., 2004. Calcium carbonate scale formation and control. Rev. Environ. Sci. Bio/Technol. 3, 159–169. http://dx.doi.org/10.1007/s11157-004-3849-1.

Martinod, A., Euvrard, M., Foissy, A., Neville, A., 2008. Progressing the understanding of chemical inhibition of mineral scale by green inhibitors. Desalination 220, 345–352. http://dx.doi.org/10.1016/j.desal.2007.01.039.

Meyer, H.J., 1984. The influence of impurities on the growth rate of calcite. J. Cryst. Growth 66, 639–646. http://dx.doi.org/10.1016/0022-0248(84)90164-7.

Mishra, Y.K., Adelung, R., 2018. ZnO tetrapod materials for functional applications. Mater. Today 21, 631–651. http://dx.doi.org/10.1016/j.mattod.2017.11.003.

Miyauchi, K., Takita, Y., Yamabe, H., Yuasa, M., 2016. A study of adhesion on stainless steel in an epoxy/dicyandiamide coating system: Influence of glass transition temperature on wet adhesion. Prog. Org. Coat. 99, 302–307. http://dx.doi.org/10.1016/j.porgcoat.2016.06.002.

Naka, K., Tanaka, Y., Chujo, Y., 2002. Effect of anionic starburst dendrimers on the crystallization of $CaCO_3$ in aqueous solution: Size control of spherical vaterite particles. Langmuir 18, 3655–3658. http://dx.doi.org/10.1021/la011345d.

Nehrke, G., Van Cappellen, P., 2006. Framboidal vaterite aggregates and their transformation into calcite: A morphological study. J. Cryst. Growth 287, 528–530. http://dx.doi.org/10.1016/j.jcrysgro.2005.11.080.

Ning, C., Mingyan, L., Weidong, Z., 2012. Fouling and corrosion properties of SiO2 coatings on copper in geothermal water. Ind. Eng. Chem. Res. 51, 6001–6017. http://dx.doi.org/10.1021/ie202091b.

Ogino, T., Suzuki, T., Sawada, K., 1987. The formation and transformation mechanism of calcium carbonate in water. Geochim. Cosmochim. Acta 51, 2757–2767. http://dx.doi.org/10.1016/0016-7037(87)90155-4.

Oral, Ç.M., Ercan, B., 2018. Influence of pH on morphology, size and polymorph of room temperature synthesized calcium carbonate particles. Powder Technol. 339, 781–788. http://dx.doi.org/10.1016/j.powtec.2018.08.066.

Parakhonskiy, B., Zyuzin, M.V., Yashchenok, A., Carregal-Romero, S., Rejman, J., Möhwald, H., Parak, W.J., Skirtach, A.G., 2015. The influence of the size and aspect ratio of anisotropic, porous CaCO3 particles on their uptake by cells. J. Nanobiotechnol. 13, 53. http://dx.doi.org/10.1186/s12951-015-0111-7.

Pardo, P., Deydier, A., Anxionnaz-Minvielle, Z., Rougé, S., Cabassud, M., Cognet, P., 2014. A review on high temperature thermochemical heat energy storage. Renew. Sustain. Energy Rev. 32, 591–610. http://dx.doi.org/10.1016/j.rser.2013.12.014.

Plummer, L.N., Busenberg, E., 1982. The solubilities of calcite, aragonite and vaterite in CO2-H2O solutions between 0 and 90 °c, and an evaluation of the aqueous model for the system CaCO3-CO2-H2O. Geochim. Cosmochim. Acta 46, 1011–1040. http://dx.doi.org/10.1016/0016-7037(82)90056-4.

Quéré, D., 2008. Wetting and roughness. Annu. Rev. Mater. Res. 38, 71–99. http://dx.doi.org/10.1146/annurev.matsci.38.060407.132434.

Ren, L.-F., Liu, C., Xu, Y., Zhang, X., Shao, J., He, Y., 2020. High-performance electrospinning-phase inversion composite PDMS membrane for extractive membrane bioreactor: Fabrication, characterization, optimization and application. J. Memb. Sci. 597, 117624. http://dx.doi.org/10.1016/j.memsci.2019.117624.

Rodriguez-Blanco, J.D., Shaw, S., Benning, L.G., 2011. The kinetics and mechanisms of amorphous calcium carbonate (ACC) crystallization to calcite, viavaterite. Nanoscale 3, 265–271. http://dx.doi.org/10.1039/C0NR00589D.

Sabzi, R., Arefinia, R., 2019. Investigation of zinc as a scale and corrosion inhibitor of carbon steel in artificial seawater. Corros. Sci. 153, 292–300. http://dx.doi.org/10.1016/j.corsci.2019.03.045.

Saulat, H., Cao, M., Khan, M.M., Khan, M., Khan, M.M., Rehman, A., 2020. Preparation and applications of calcium carbonate whisker with a special focus on construction materials. Constr. Build. Mater. 236, 117613. http://dx.doi.org/10.1016/j.conbuildmat.2019.117613.

Schindelin, J., Arganda-Carreras, I., Frise, E., Kaynig, V., Longair, M., Pietzsch, T., Preibisch, S., Rueden, C., Saalfeld, S., Schmid, B., Tinevez, J.-Y., White, D.J., Hartenstein, V., Eliceiri, K., Tomancak, P., Cardona, A., 2012. Fiji: an open-source platform for biological-image analysis. Nature Methods 9, 676–682. http://dx.doi.org/10.1038/nmeth.2019.

Schneider, C.A., Rasband, W.S., Eliceiri, K.W., 2012. NIH Image to ImageJ: 25 years of image analysis. Nature Methods 9, 671–675. http://dx.doi.org/10.1038/nmeth.2089.

Tagomori, K., Kioka, A., Nakagawa, M., Ueda, A., Sato, K., Yonezu, K., Anzai, S., 2022. Air nanobubbles retard calcite crystal growth. Colloids Surf. A 648, 129319. http://dx.doi.org/10.1016/j.colsurfa.2022.129319.

Tang, Y., Yang, W., Yin, X., Liu, Y., Yin, P., Wang, J., 2008. Investigation of CaCO3 scale inhibition by PAA, ATMP and PAPEMP. Desalination 228, 55–60. http://dx.doi.org/10.1016/j.desal.2007.08.006.

Tegladza, I.D., Lin, G., Liu, C., Gu, X., 2023. Control of crystal nucleation, size and morphology using micro-/nanobubbles as green additives – a review. Sep. Purif. Technol. 311, 123232. http://dx.doi.org/10.1016/j.seppur.2023.123232.

Trushina, D.B., Bukreeva, T.V., Kovalchuk, M.V., Antipina, M.N., 2014. $CaCO_3$ vaterite microparticles for biomedical and personal care applications. Mater. Sci. Eng. C 45, 644–658. http://dx.doi.org/10.1016/j.msec.2014.04.050.

Wada, N., Yamashita, K., Umegaki, T., 1995. Effects of divalent cations upon nucleation, growth and transformation of calcium carbonate polymorphs under conditions of double diffusion. J. Cryst. Growth 148, 297–304. http://dx.doi.org/10.1016/0022-0248(94)00880-9.

Wang, Z.L., 2004. Zinc oxide nanostructures: growth, properties and applications. J. Phys.: Condens. Matter 16, R829–R858. http://dx.doi.org/10.1088/0953-8984/16/25/R01.

Wang, H., Alfredsson, V., Tropsch, J., Ettl, R., Nylander, T., 2013. Formation of CaCO3 deposits on hard surfaces—Effect of bulk solution conditions and surface properties. ACS Appl. Mater. Interfaces 5, 4035–4045. http://dx.doi.org/10.1021/am401348v.

Wei, W., Ma, G.-H., Hu, G., Yu, D., Mcleish, T., Su, Z.-G., Shen, Z.-Y., 2008. Preparation of hierarchical hollow CaCO3 particles and the application as anticancer drug carrier. J. Am. Chem. Soc. 130, 15808–15810. http://dx.doi.org/10.1021/ja8039585.

Wen, T., Zhao, Y., Zhang, T., Xiong, B., Hu, H., Zhang, Q., Song, S., 2020. Selective recovery of heavy metals from wastewater by mechanically activated calcium carbonate: Inspiration from nature. Chemosphere 246, 125842. http://dx.doi.org/10.1016/j.chemosphere.2020.125842.

Wolf, M.P., Salieb-Beugelaar, G.B., Hunziker, P., 2018. PDMS with designer functionalities—Properties, modifications strategies, and applications. Prog. Polym. Sci. 83, 97–134. http://dx.doi.org/10.1016/j.progpolymsci.2018.06.001.

Wu, P., Cui, P., Du, H., Alves, M.E., Liu, C., Zhou, D., Wang, Y., 2019. Dissolution and transformation of ZnO nano- and microparticles in soil mineral suspensions. ACS Earth Space Chem. 3, 495–502. http://dx.doi.org/10.1021/acsearthspacechem.8b00165.

Yamauchi, Y., Tenjimbayashi, M., Samitsu, S., Naito, M., 2019. Durable and flexible superhydrophobic materials: Abrasion/scratching/slicing/droplet impacting/bending/twisting-tolerant composite with porcupinefish-like structure. ACS Appl. Mater. Interfaces 11, 32381–32389. http://dx.doi.org/10.1021/acsami.9b09524.

Yan, W., Lin-lin, W., Ming-yan, L., 2007. Antifouling and enhancing pool boiling by TiO2 coating surface in nanometer scale thickness. AIChE J. 53, 3062–3076. http://dx.doi.org/10.1002/aic.11345.

Zhang, Y., Chen, Y., Westerhoff, P., Hristovski, K., Crittenden, J.C., 2008. Stability of commercial metal oxide nanoparticles in water. Water Res. 42, 2204–2212. http://dx.doi.org/10.1016/j.watres.2007.11.036.

Zhang, Y., Duan, H., Chen, E., Li, M., Liu, S., 2023. Physicochemical characteristics and the scale inhibition effect of air nanobubbles (A-NBs) in a circulating cooling water system. Langmuir 39, 1629–1639. http://dx.doi.org/10.1021/acs.langmuir.2c03075.

Zhang, J., Pu, G., Severtson, S.J., 2010. Fabrication of zinc oxide/polydimethylsiloxane composite surfaces demonstrating oil-fouling-resistant superhydrophobicity. ACS Appl. Mater. Interfaces 2, 2880–2883. http://dx.doi.org/10.1021/am100555r.

Zhao, Y., Luo, Z., Li, M., Qu, Q., Ma, X., Yu, S.-H., Zhao, Y., 2015. A preloaded amorphous calcium carbonate/doxorubicin@silica nanoreactor for pH-responsive delivery of an anticancer drug. Angew. Chem. Int. Ed. 54, 919–922. http://dx.doi.org/10.1002/anie.201408510.

Zhou, D., Keller, A.A., 2010. Role of morphology in the aggregation kinetics of ZnO nanoparticles. Water Res. 44, 2948–2956. http://dx.doi.org/10.1016/j.watres.2010.02.025.

Zhou, G.-T., Yao, Q.-Z., Fu, S.-Q., Guan, Y.-B., 2010. Controlled crystallization of unstable vaterite with distinct morphologies and their polymorphic transition to stable calcite. Eur. J. Mineral. 22, 259–269. http://dx.doi.org/10.1127/0935-1221/2009/0022-2008.